(7) M. Matsuo and R. St. J. Manley, *Macromolecules*, **15**, 985 (1982).
(8) P. Smith and P. J. Lemstra, *J. Mater. Sci.*, **15**, 505 (1980).
(9) P. Smith and P. J. Lemstra, *Makromol. Chem.*, **180**, 2983 (1979).
(10) P. Smith and P. J. Lemstra, *Colloid Polym. Sci.*, **258**, 891 (1980).
(11) P. Smith, P. J. Lemstra, and H. C. Booij, *J. Polym. Sci., Polym. Phys. Ed.*, **19**, 877 (1981).
(12) P. Smith, P. J. Lemstra, J. P. L. Pijpers, and A. M. Kiel, *Colloid Polym. Sci.*, **259**, 1070 (1981).
(13) M. Matsuo and R. St. J. Manley, *Macromolecules*, **16**, 1500 (1983).
(14) D. J. Blundell, *Acta Crystallogr., Sect. A*, **26**, 472 (1970).
(15) D. J. Blundell, *Acta Crystallogr., Sect. A*, **26**, 476 (1970).
(16) T. Hashimoto, K. Nagatoshi, A. Todo, H. Hasegawa, and H. Kawai, *Macromolecules*, **7**, 364 (1974).
(17) M. Matsuo, C. Sawatari, M. Tsuji, and R. St. J. Manley, *J. Chem. Soc., Faraday Trans. 2*, in press.
(18) D. Ya. Tsvankin, *Polym. Sci. USSR (Engl. Transl.)*, **6**, 2304 (1964).
(19) B. Crist, *J. Polym. Sci., Polym. Phys. Ed.*, **11**, 635 (1973).

Phase Contrast Imaging of Styrene–Isoprene and Styrene–Butadiene Block Copolymers

Dale L. Handlin, Jr.,† and Edwin L. Thomas*

Department of Polymer Science and Engineering, University of Massachusetts, Amherst, Massachusetts 01003. *Received November 10, 1982*

ABSTRACT: Phase contrast produced in the electron microscope by defocus techniques has been used to obtain the first *unstained* images of styrene–isoprene and styrene–butadiene diblock and triblock copolymers. Theoretical image calculations based on square-wave and circular cross section one-dimensional models were used to demonstrate the effects of mean inner potential difference, interface width, and microscope optics on resultant images. Experimental phase contrast images of microtomed block copolymers with ordered lamellar, cylindrical, and disordered spherical morphologies were in good agreement with theory and with experimental scattering contrast images (osmium tetraoxide stain). Repeat periods in the ordered morphologies were found to be independent of the microscope parameters as theoretically predicted. Calculations show that the compositional profile across the interface between the polymer phases will not be easily measured from experimental phase contrast images because of the smoothing effect of limited electron beam coherence. The phase contrast technique is, however, sufficient to visualize the phase-separated regions of polymers of quite similar atomic composition and/or density, eliminating the need for chemical modification of one or both of the polymers.

Introduction

Historically, transmission electron microscopy (TEM) has been the principal technique for determining the morphology of styrene–isoprene (SI) and styrene–butadiene (SB) block copolymers. These copolymers represent the large class of phase-separated copolymers, blends, and graft copolymers whose phases are so similar in chemical composition and density that the phases have only been distinguished by the introduction of highly reactive, selective reagents, such as osmium tetraoxide, which bind to or degrade one phase to provide scattering contrast. Phase[24] contrast, however, is much more sensitive to small differences between the two phases which are reflected in their mean inner potentials, permitting phase contrast imaging utilizing electron microscope transfer theory and making staining unnecessary for many polymer systems.

Petermann and Gleiter[1] found negligible scattering contrast between amorphous regions and nondiffracting crystallites in polyethylene films and were the first to employ *phase contrast* for imaging polymer systems. The mean inner potential difference (the mean inner potential (measured in volts) is analogous to the refractive index in light optical phase contrast microscopy) of 1.03 V between crystalline and amorphous regions in polyethylene provided ample phase contrast in films only 10–30 nm thick (see Table I for a listing of mean inner potentials of common polymers). Polystyrene and polyisoprene show a significantly smaller difference in potential of 0.61 V. The potential difference between polystyrene and polybutadiene ranges from 0.08 V (negligible) for 100% 1,4-*cis*-polybutadiene to 0.76 V for 44% 1,4-*cis*-, 42% 1,4-*trans*-, and 14% 1,2-polybutadiene. Therefore block copolymers of SI and certain SB's should be imagable without staining using phase contrast, although with much lower contrast than for polyethylene.

Table I
Mean Inner Potentials of Common Polymers

polymer	density, g/cm³	mean inner potential, V
polystyrene	1.05	7.08
polyisoprene	0.904	6.47
poly(1-butene)	0.87	6.40
polybutadiene		
1,2	0.90	6.35
1,4 (cis)	0.895	7.13
44% 1,4 cis, 42% 1,4 trans, 14% 1,2	0.895	6.32
polyethylene		
crystal	1.00	7.35
amorphous	~0.86	6.32

The objective of this paper is to demonstrate that even in the absence of crystallinity, phase-separated copolymers of very similar density and composition can be imaged by phase contrast techniques without resorting to stains, which are often artifact inducing, time-consuming, and hazardous to use. Regular SI and SB block copolymers were chosen as model systems because they phase separate in three well-defined morphologies: lamellar, cylindrical, and spherical. Using the transfer theory of imaging, one can predict the phase contrast images of these morphol-

† Present address: Westhollow Research Center, Shell Development Co., Houston, TX 77001.

0024-9297/83/2216-1514$01.50/0

ogies using numerical Fourier transform techniques of simple one-dimensional models. Because phase contrast arises from the interfaces between the phases, diffuse interfaces of different widths will be included in the model calculations in order to determine whether interface widths can be measured from the experimental images.

Reviews of the transfer theory of electron microscope imaging have been given by Hanszen,[2] Erickson,[3] Misell,[4,5] and Cowley.[6] Christner and Thomas[7] adapted the theory to polymer applications and Roche and Thomas[8] have recently verified their predictions experimentally. For brevity, the present paper omits all detailed treatment of the transfer theory and the interested reader is referred to the above references.

Image calculations and experimental images will be presented for the following polymers: a lamellar ISI triblock, a lamellar SBS triblock, a cylindrical SIS triblock, and a 12-arm SI star block copolymer with large spherical phases lacking long-range order. The lamellar morphologies provide the simplest projections and are thus expected to have the highest contrast. The first lamellar system is an ISI triblock copolymer that has been highly oriented in shear, while the second, a SBS triblock, was compression molded and exhibits much less order. The cylindrical morphology is particularly interesting because it contains two simple projections: a transverse section with interfaces parallel to the electron beam and a longitudinal section with interfaces curved with respect to the beam. The star block copolymer is included because it contains large enough spherical phases (up to 200 nm in diameter) providing thick sections with simple projections of the two phases which should exhibit detectable scattering contrast. Such samples will allow the examination of both phase and scattering contrast in a single image. Images of an ordered spherical polymer will be presented in a future paper.[22] Image calculations for the lamellar and transversely cut cylindrical morphology are carried out by using a square wave convoluted with a smoothing function to provide a projected diffuse interface model. The longitudinal projection of the cylindrical morphology and the spherical morphology are modeled by a projection of circles.

Experimental Section

Polymers. The SBS lamellar block copolymer is Shell's sample TR-41-1649. The viscosity-average molecular weights of the blocks are 14 000–30 000–14 000 and the weight fractions 0.24–0.52–0.24. The microstructure of the butadiene is 40 mol % cis 1,4, 50% trans 1,4, and 10% 1,2.[9] The films were hot pressed at 130 °C followed by slow cooling to room temperature.

The ISI triblock has a total molecular weight M_n = 48 500 ± 4000 and $M_w/M_n \approx 1.2$ as determined by GPC with a styrene weight fraction of 47.4% by ultraviolet measurements. The cylindrical SIS triblock has M_n = 105 000 ± 8000 and M_w/M_n = 1.18 by GPC with a weight fraction of polystyrene of 25.7% by UV. These two polymers were provided by G. Hadziioannou. Their synthesis and characterization by SAXS and SANS have been described previously by Hadziioannou et al.[10-12] Both polymers had been highly oriented in shear so that the lamellar and cylinder axes lie in the plane of the film.[13]

The star copolymer consists of 12 arms, each being an identical SI block copolymer (the isoprene blocks are at the center of the star) having segment molecular weights M_n = 63 400 (PI)–28 700 (PS), M_w/M_n = 1.08, and weight fraction of polystyrene 31%. This polymer was supplied by Bi and Fetters, who have previously described its synthesis.[14] The sample was prepared for microtoming by slow evaporation from a 10% toluene solution over a period of days followed by annealing at 120 °C for 5 days.

Cryoultramicrotoming. All four *unstained* samples were microtomed at low temperature (−80 to −120 °C) with a Reichert Ultracut microtome fitted with an FC-4 cold stage. The technique used for collecting thin sections from the knife edge was similar to that used by Odell et al.[15]

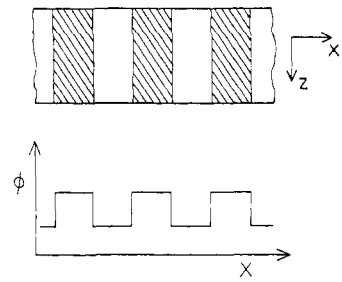

Figure 1. One-dimensional model of the projected mean inner potential of a pure two-phase system having interfaces parallel to the incident beam direction (Z).

Some sections were osmium tetraoxide stained *after* sectioning by exposing the grid to vapor from a 3% aqueous solution at room temperature for 4 h.

Electron Microscopy. The microscope used was a JEOL 100 CX with a side-entry goniometer. Magnification calibration was performed by using catalase crystals which were themselves calibrated by electron diffraction comparison to polycrystalline gold. The error from this method of calibration has been estimated to be 2.5%.[16]

Spacings in the images were measured by using a Polaron optical bench. Error due to lens distortion on the optical bench is estimated to be 2%. Additional errors of about 1% arise from improper positioning of the sample relative to the center of the objective lens. The total uncertainty in the spacings quoted from the micrographs should be less than 6% and the relative spacings in the same micrograph should be accurate to 2%.

Phase Contrast Image Calculations

Lamellar Model. Figure 1 is a one-dimensional model of the projected mean inner potential of phase-separated SI or SB lamellar copolymers having sharp interfaces parallel to the incident beam. This choice of model was based on SAXS results of Hadziioannou et al. on the ISI triblock[12] and on results of Hashimoto et al. on the SBS triblock.[9] The long period is 28 nm with equal phase widths. The relative change in phase of the electron wave after passing through regions of different potential in the object is given by

$$\Delta\psi = \frac{\pi}{\lambda V_0} t \Delta\phi$$

where λ is the electron wavelength (0.0037 nm at 100 kV), V_0 is the accelerating voltage, t is the sample thickness, and $\Delta\phi$ is the mean inner potential difference between polymer phases. A relative phase shift $\Delta\psi$ of 0.5 rad was chosen for all calculations since it represents the relative phase difference for a wave passing through adjacent styrene and rubber phases in an approximately 100-nm-thick film. This is the relative phase shift between the parts of the wave passing through the two phases and not the magnitude of the shift from the unscattered wave. The phase shift profile is analogous to the electron density profile used in SAXS and defines the object function $F_0(r_0)$. Diffuse boundaries may be introduced by convolution of $F_0(r_0)$ with a smoothing function $h(r_0)$:

$$F_0(r_0) = h(r_0) * F_0(r_0) \quad (1)$$

The smoothing function usually chosen in SAXS is a Gaussian, $\exp(-\sigma^2 r_0^2)$, where σ is the standard deviation, because of its mathematical simplicity. On the basis of the Cahn and Hilliard theory of inhomogeneous liquids,[17] however, Helfand[18] has proposed the interface profile

$$F_0(r_0) = \tanh(2r_0/t) \quad (2)$$

where the interface thickness t is given by $t = (2\pi)^{1/2}\sigma$. The thickness, t, used as a measure of interface width, is

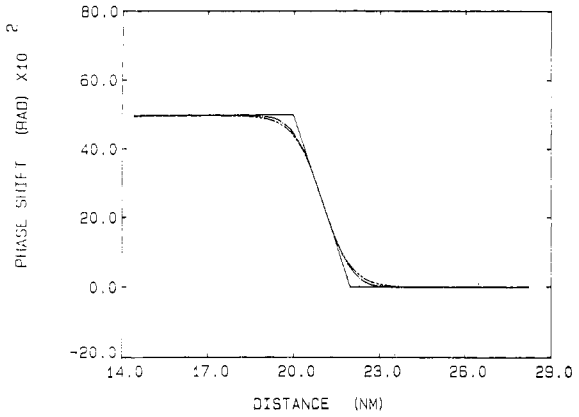

Figure 2. Comparison of (—) ramp, (-·-) Gaussian, and (- - -) hyperbolic tangent interfaces for t = 2.0 nm.

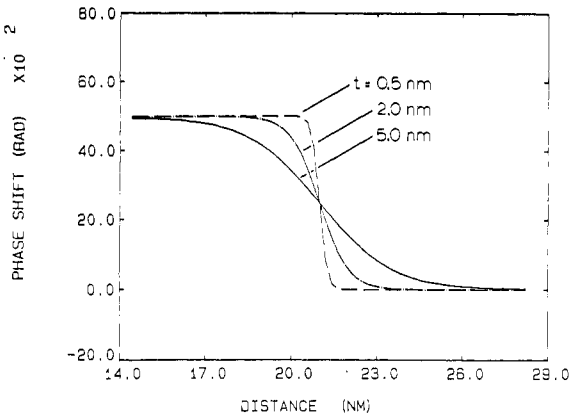

Figure 3. Hyperbolic tangent interface widths used for image calculations.

the width of a ramp interface having the same slope at the center of the interface as eq 2.

Figure 2 shows that the hyperbolic tangent interface profile is only slightly smoother than the Gaussian profile for t = 2.0 nm. The hyperbolic tangent interface will be used for further calculations because it has the soundest theoretical background for block copolymers and has, as well, proven to be essentially indistinguishable from the Gaussian interface for our calculated images. Figure 3 compares the hyperbolic tangent profiles of width 0.5, 2.0, and 5.0 nm. Interfaces sharper than about 0.5 nm are physically unrealistic and those wider than about 5 nm begin to significantly alter the phase compositions for this model.

The effect of interface width is best seen in the diffraction patterns in Figure 4 calculated by a fast Fourier transform computer program. The width and magnitude of the various diffraction peaks depend on the number of repeats used in the object model. Four repeat units were found to give essentially infinitely sharp (in the resolution of the data) peaks while requiring a manageable amount of computer time. The scattered intensity in Figure 4 is the product of the squares of the form factor of the scatterers and the lattice factor. Therefore, for this model with equal phase width (50–50 composition), the even orders in the diffraction pattern are absent because the form factor $\sin(\pi TS)/(\pi S)$, where T is the phase width ($^1/_2$ the repeat period) passes through zero at $S = n/T$ (n an integer). The SAXS pattern of the SBS copolymer in Figure 5 shows that the second order is indeed absent, confirming the equal phase width in this polymer.

As Figure 4 shows, the effect of diffuse interfaces is to strongly damp the high-angle scattered intensity so that only the first and third orders have appreciable intensity

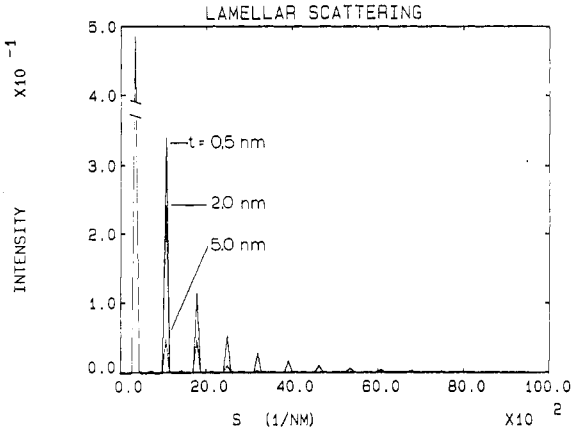

Figure 4. Calculated diffracted intensity from models in Figure 3. Zero-order peak is not shown.

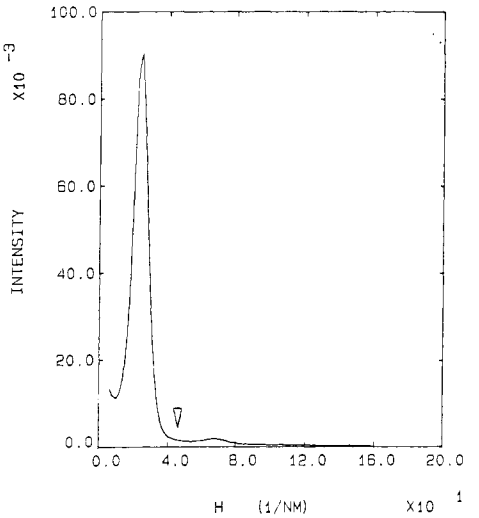

Figure 5. Smeared SAXS intensity vs. h for the SBS lamellar block copolymer. Arrow points to the position of the absent second order.

for the 5-nm interface. For the image calculation, this diffraction pattern is multiplied by the microscope pupil function and the product is then Fourier transformed. The pupil function represents the deviation of the microscope optics from ideality (the ideal pupil function would be unity for all frequencies) and includes effects such as spherical aberration, chromatic aberration, beam coherence, and, most importantly, defocus (ΔZ, the distance in nm of the focal plane of the objective lens from the plane of the object). For an ideal transfer function the contrast in the image is simply $2\Delta\psi$. Since the actual microscope pupil function is zero at small angles for small defocus (i.e., microscope operated for high resolution), with the maximum moving to smaller angles with increasing defocus, one should find large differences in image contrast at small defocus as a function of interface width. Figure 6a shows the range of frequencies in the diffraction pattern of the 2-nm interface model that will be strongly transferred to the image by a pupil function with defocus, ΔZ, of -1.0 μm. The calculated images in Figure 6b for $\Delta Z = -1.0$ μm are indeed strongly dependent on interface width. Therefore one should be able to measure the interface width from the absolute contrast level at small defocus. There are, however, two important factors that affect the experimental contrast that are not included in these theoretical calculations: inelastic scattering and beam coherence. The number of inelastically scattered electrons increases rapidly with sample thickness. Misell[4] has calculated that ~70%

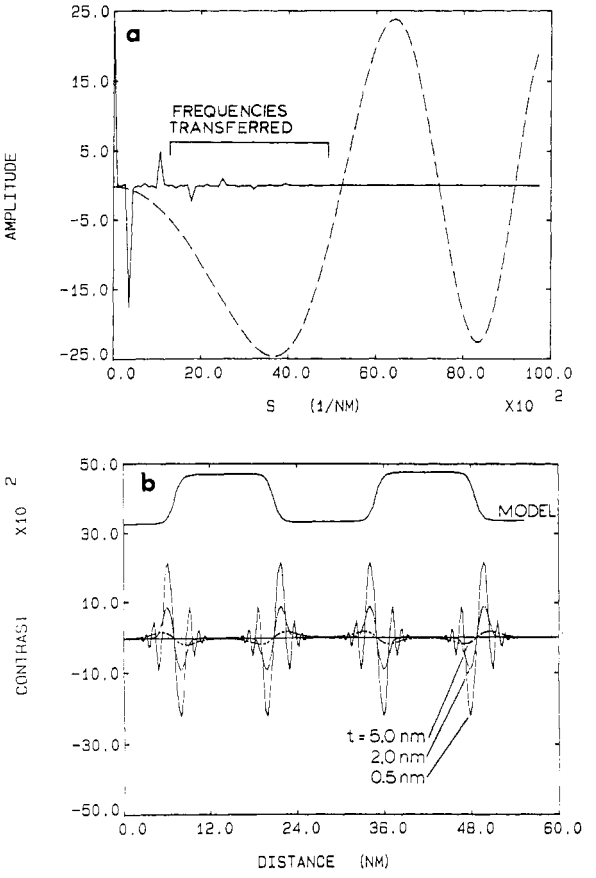

Figure 6. (a) Pupil function (dashed curve) for $\Delta Z = -1.0$ μm and $\alpha = 10^{-4}$ rad overlaid on the calculated scattered *amplitude* from the $t = 2.0$ nm model. (b) Calculated images of the three models from Figure 3 at $\Delta Z = -1.0$ μm and $\alpha = 10^{-4}$ rad. Negative contrast corresponds to dark regions in the image.

of a 100-kV beam is inelastically scattered by a 100-nm-thick biological specimen. These inelastically scattered electrons suffer chromatic aberration, resulting in a large additional and variable phase shift so that the inelastic image contributes a blurred, out-of-focus background. In addition, the mean free path for elastic scattering of a 100-kV electron is about 100 nm in carbon so that above this thickness many of the elastically scattered electrons may undergo multiple scattering, either elastic or inelastic, and be removed from the coherent elastic signal (which gives the desired phase contrast image). Thus the effect of inelastic and multiple scattering will be to raise the overall dc level of image intensity and thus to decrease the contrast by a factor of 3–4, for a 100-nm-thick film.[4]

A tungsten hairpin filament can be represented as a partially coherent electron source characterized by the illumination half-angle α. Unfortunately, the effect of beam coherence is similar to that of diffuse interfaces in damping the diffracted intensity at high angles: the poorer the coherence, the stronger the damping (see Figure 7). An illumination half-angle of $\alpha = 10^{-4}$ rad is probably the lower limit that is experimentally useful with a tungsten hairpin filament source. Angles of 5×10^{-4} to 1×10^{-3} rad are not at all unusual in practice and will cause increased damping of the small-defocus images, resulting in an effect very similar to broad interfacial width as can be seen by comparing Figures 6 and 7. For these reasons, we would not expect any experimentally detectable contrast in the present work for small-defocus conditions where interface widths are measurable.

Contrast can be increased by increasing the defocus until the first maximum of the pupil function coincides with the

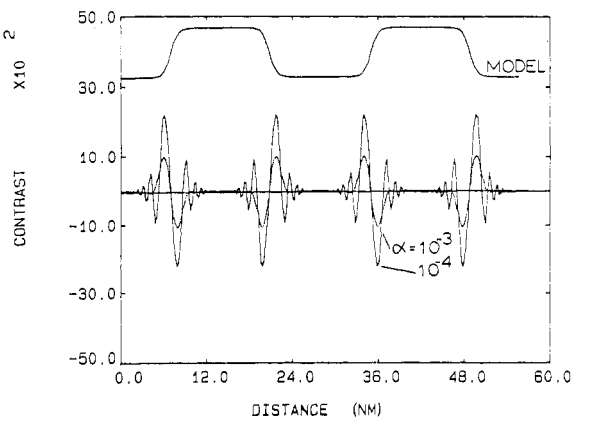

Figure 7. Images of the $t = 0.5$ nm model at $\Delta Z = -1.0$ μm for two illumination angles.

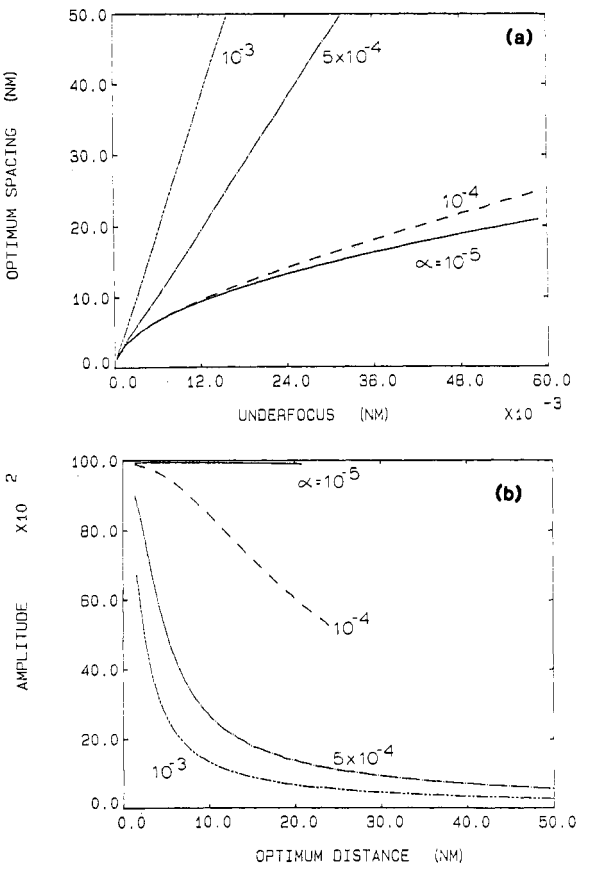

Figure 8. (a) Distance corresponding to the first maximum of the pupil function for underfocuses from −0.3 to −60 μm for different values of α. (b) Amplitude of the first maximum of the pupil function for the distances shown in figure for different values of α.

reciprocal space frequency for the repeat spacing d of the particular model. For large defocuses, $\Delta Z_{opt} \simeq -d^2/2\lambda$. For large object periods, this will require very high defocuses and the position and amplitude of the first maximum of the pupil function will be significantly affected by finite beam coherence, making it impossible to find an "optimum defocus" for a period greater than about 20 nm. Figure 8a shows a plot of the required amount of underfocus to optimally transfer various object distances for several coherence conditions. The decreased amplitude of the pupil function with beam coherence is shown in Figure 8b. For example, a model with a 10-nm period assuming perfect coherence requires a defocus of about 14 μm, for which the amplitude of the pupil function is −1.0, whereas for a coherence of 1×10^{-3} rad, the required defocus is only 3 μm

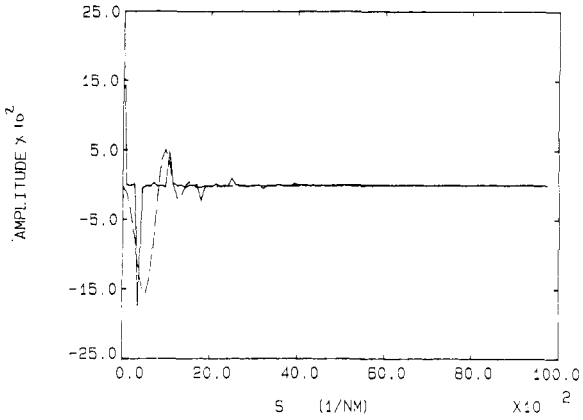

Figure 9. Pupil function (dashed curve) for $\Delta Z = -40$ μm and $\alpha = 10^{-4}$ rad, overlaid on the calculated scattered amplitude from the $t = 2.0$ nm model.

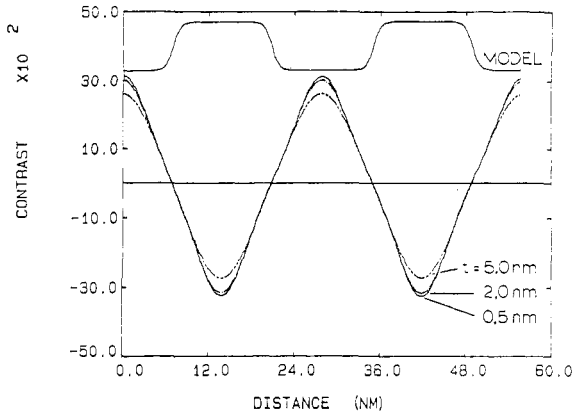

Figure 10. Calculated images of the three models in Figure 3 at $\Delta Z = -40$ μm and $\alpha = 10^{-4}$ rad.

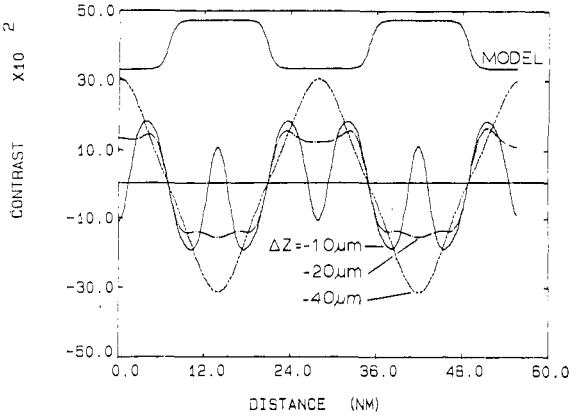

Figure 11. Calculated images from the $t = 2.0$ nm model for different defocuses and $\alpha = 10^{-4}$ rad.

but the amplitude of the pupil function has fallen to −0.16.

Figure 9 shows the transfer function for $\Delta Z = -40$ μm with $\alpha = 1 \times 10^{-4}$ rad overlaid on the diffracted amplitude of the 28-nm period–2.0-nm interface model. As Figure 10 shows, there is ample contrast between the respective polymer phases at 40-μm underfocus. However, the effect of the model interface width on the various calculated image profiles is negligible. The inability to distinguish the interface profile results from the loss of image resolution caused by the large value of defocus employed. The image resolution can be estimated from the value of the object frequency at which the transfer function reaches zero (about 5.5 nm for $\Delta Z = -40$ μm).

Figure 11 demonstrates the change in image contrast as a function of defocus for the 2-nm interface model. A

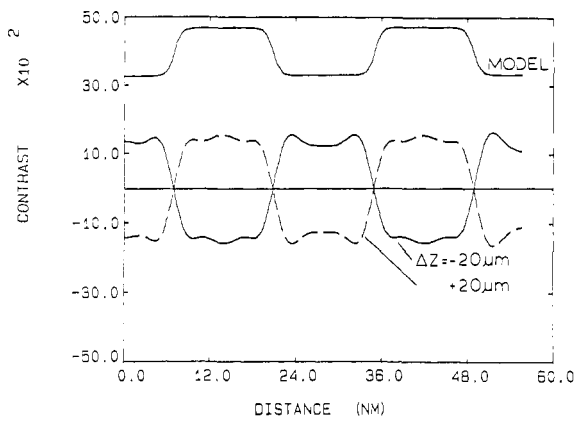

Figure 12. Calculated images for underfocus and overfocus conditions. $t = 2.0$ nm and $\alpha = 10^{-4}$ rad.

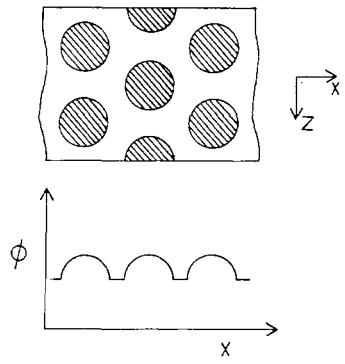

Figure 13. One-dimensional model of the normalized projected mean inner potential variation of a pure two-phase system with a circular cross section dispersed phase.

gradual transition occurs from the pair of dark–light fringes at each interface at small defocus (recall Figure 6b) to a single dark fringe in the styrene phase and a light fringe in the rubber phase in the largest defocus image. Notice that at $\Delta Z = -10$ μm, the dark–light fringes are evenly spaced, resulting in false half-fringes in the center of the phase. Since $\Delta Z = -10$ μm is the optimum defocus for a 9-nm spacing ($^1/_3$ and not $^1/_2$ of the model repeat period), this half-fringe is not an optimum defocus effect but results from the distance of the fringe center from the interface, which is a function of defocus. The model only serves to define the distance between neighboring interfaces. Such false half-spacings were first predicted by the image calculations of Roche and Thomas[7] and observed experimentally by Petermann in polyethylene films.[19] False half-spacings could also be produced by an optimum defocus effect if the diffraction pattern of the model contained sufficient intensity in the second order, which is absent for this particular model. Beyond a defocus of −20 μm, where the fringes coalesce, a simple image is obtained that continues to increase in contrast with defocus since there is no optimum defocus for a 28-nm spacing as shown by Figure 8.

The above calculations have employed only underfocus because the phase contrast produced by underfocus is negative (dark) in the higher potential phase and positive (light) in the lower potential phase. At large defocuses, where $\Delta Z \gg C_s\lambda^2/2$ (C_s is the spherical aberration coefficient of the objective lens), overfocus and underfocus are antisymmetric so that the phase contrast exactly reverses on changing from underfocus to overfocus as demonstrated in Figure 12.

For very small defocuses (less than $\sim$0.5 μm) the transfer function is approximately zero to relatively large scattering angles. Therefore, large- and medium-scale

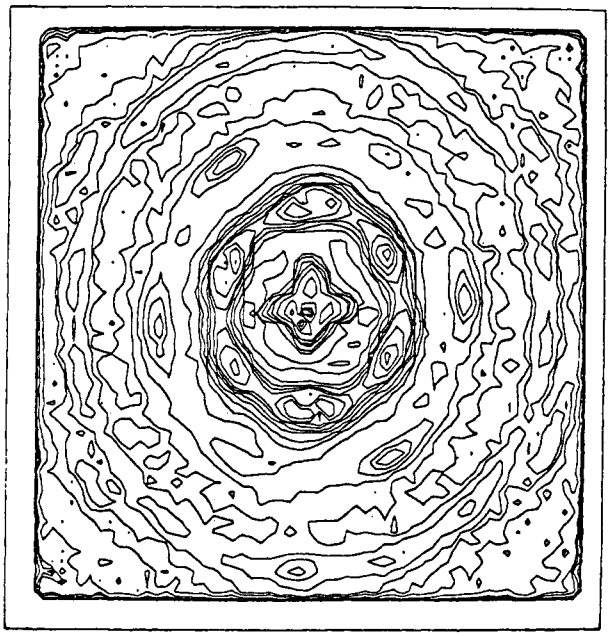

Figure 14. Two-dimensional SAXS pattern (ORNL) of an SIS triblock copolymer containing hexagonally packed styrene cylinders in an isoprene matrix. Successive isointensity contours are double the previous intensity level.

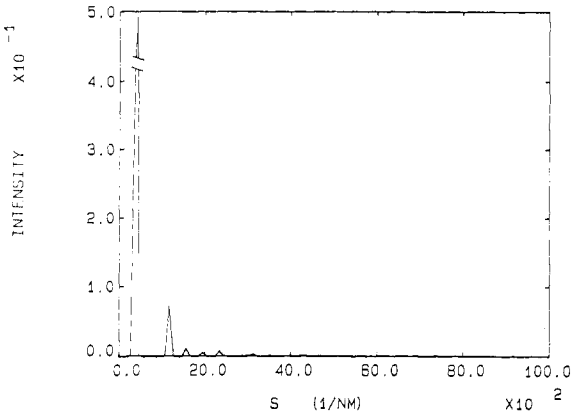

Figure 15. Calculated diffracted intensity from the circular model in Figure 13. Zero-order peak is not shown.

phase contrast will be negligible at zero defocus. The term "zero defocus" is used here to mean the point of minimum phase contrast, although minimum contrast actually occurs at $\Delta Z \simeq -50$ nm for our JEOL 100 CX with $C_s = 6.7$ mm.

Circular Projection Model. The circular projections in Figure 13 were used to model the longitudinal cylinder projection. This one-dimensional projection serves as a qualitative model for spheres as well, although proper image calculations would require a two-dimensional projection. The size and spacings of the circles were approximately matched to the SAXS pattern of the SIS cylindrical triblock shown in Figure 14. The hexagonal SAXS pattern is slightly deformed (sample was taken from edge of plaque), giving spacings of 26.8, 24.5, and 27.6 ± 1.0 nm, in good agreement with Hadziioannou's[13] value from a truly hexagonal pattern of 26.3 ± 0.3 nm. The cylinder radius was calculated to be 8.0 nm from the known volume fraction of styrene. The difference in phase shift was arbitrarily set to 0.5 rad for comparison to the lamellar model; however, since the cylinders are 30 nm apart in the vertical direction, the contrast in the calculated images should be divided by 3.5 for comparison to experimental images. The effect of interface width has not been included in this model because the smoothing convolution

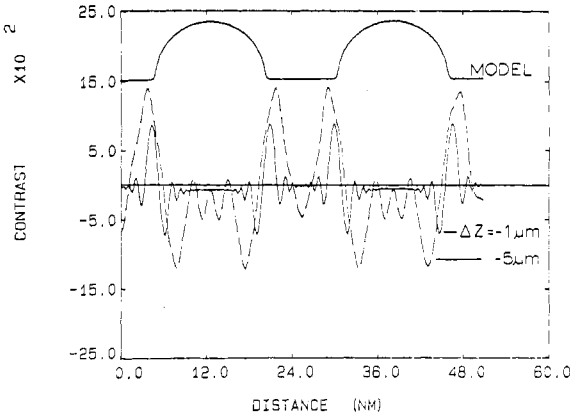

Figure 16. Calculated images for the circular model at small defocuses, $\alpha = 10^{-4}$ rad.

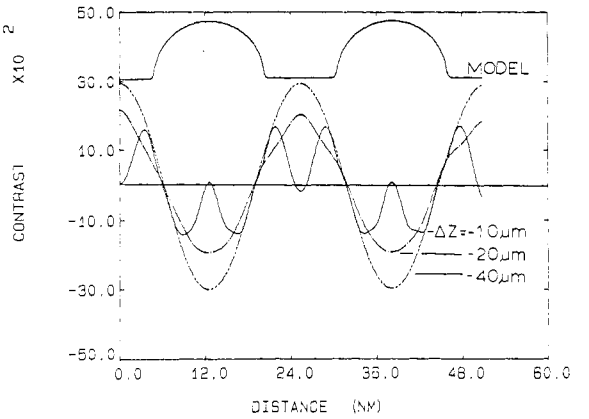

Figure 17. Calculated images for the circular model at large defocuses, $\alpha = 10^{-4}$ rad.

would have to be done in two dimensions before projection into the one-dimensional model in Figure 13. The diffraction pattern for this model is shown in Figure 15. The overall contrast level at small defocuses (see Figure 16) is lower than with the square-wave interface since the circle has a more rapidly decreasing form factor for equal cross-sectional dimensions. As defocus is increased (see Figure 17) the fringes in the circle phase merge at about $\Delta Z = -20$ μm. False half-fringes will probably not be apparent in the experimental image because the contrast at the defocus at which they occur is too low. Notice that the contrast does not pass through zero at the midpoint of the interface for the small defocuses in Figure 16 as it did for all defocuses of the lamellar model. This is a result of the increasing influence of the periodic nature of the model relative to the high-resolution detail (interfaces) with increasing defocus. At high defocus (see Figure 17) the phase contrast image appears very similar to that of the square-wave model, giving the appearance of two equal width phases. This results from the fact that essentially only one reciprocal space frequency is retained in large-defocus images, giving the image a cosine wave appearance.

The calculations for the cylindrical model therefore predict that the contrast will continue to increase with increasing defocus as in the lamellar model. Unlike the lamellar model, however, the apparent phase sizes will be a function of defocus.

Scattering Contrast. Misell and Burdett have shown that the bright-field image intensity of an amorphous material is given by[20]

$$I = I_0 \exp(-S_p \rho t_0) \tag{3}$$

where ρ and t_0 are the sample density and thickness and

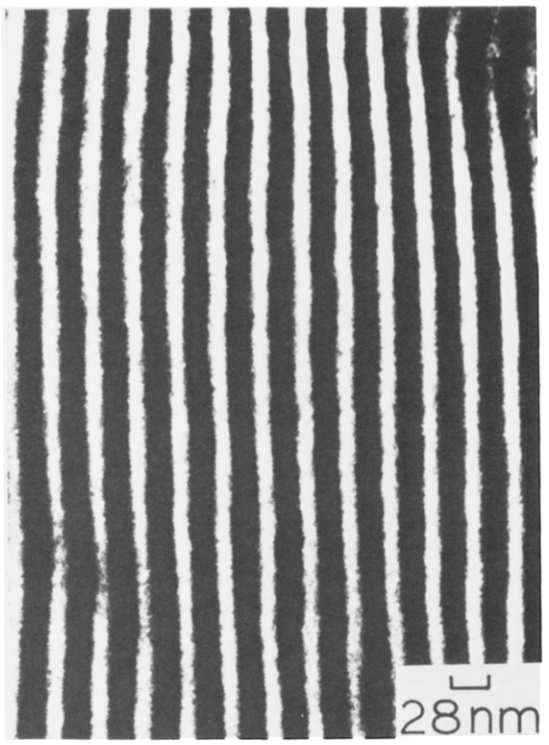

Figure 18. Bright-field (BF) image of osmium tetraoxide stained ISI lamellar copolymer (dark, isoprene; light, styrene).

S_p is a function only of the accelerating voltage and the angular limit of scattering as defined by the objective aperture half-angle. S_p values for the nominal 200-, 100-, and 20-μm objective apertures employed were measured by reference to polystyrene latex spheres of various diameters supported on a thin polystyrene film. Since the density of the spheres and the support and the diameter (hence the thickness) of the spheres are known, the only variables are S_p and the thickness of the support. Given two or more sphere sizes, both variables can be determined. For a SI or SB copolymer 100 nm thick in which both phases are continuous through the thickness of the film, the scattering contrast with the 100-μm aperture (S_p = 0.0059 ± 0.0004 cm^3/(nm g)) should be ~5%. This value is approximately the minimum contrast necessary for imaging in the absence of phase contrast (i.e., at zero defocus). It should therefore be added to (for underfocus) or subtracted from (for overfocus) the phase contrast in the defocus images.

Summary of Calculations. In summary, the calculations for the square-wave and circular models demonstrate that the phase contrast is strongly dependent on defocus and beam coherence and for a given condition of defocus, and coherence depends on three factors: (1) the difference in mean inner potential between the phases; (2) the distance between interfaces [this distance determines how much fringes from neighboring interfaces overlap at a given defocus]; and (3) the repeat period of the model.

Perhaps the most important result is that the repeat period in the image is *independent of defocus* and equal to that in the object. If the phases are not equal in size, however, the individual phase widths *are a function of defocus*.

Experimental Results and Discussion

ISI Lamellar Copolymer. An image of the osmium tetraoxide stained ISI lamellar copolymer (scattering contrast; zero defocus) is shown in Figure 18. Although the spacings in this image agree with the SAXS spacing found by Hadziioannou et al.,[13] such exact agreement was the exception rather than the rule. Spacings ranged from 16 to 34 nm, depending on the angle of the plane of the lamellae to the microtome knife and the tilt angle of the interface to the electron beam. Tilting the interfaces away from parallel to the beam should increase the apparent spacing by secant (tilt angle). Smaller spacings than the "true spacing" must therefore be due to deformation in microtoming.

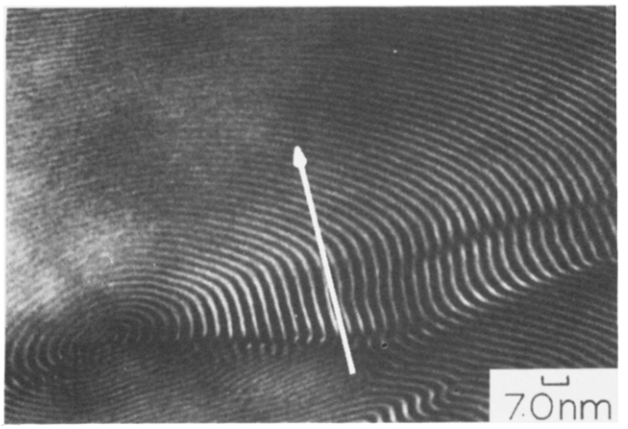

Figure 19. BF image of osmium tetraoxide stained ISI lamellar copolymer. Arrow indicates microtoming direction.

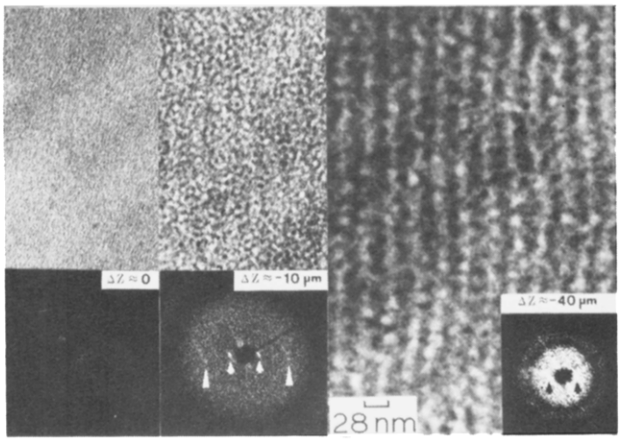

Figure 20. Underfocus series of BF images of the unstained ISI lamellar copolymer. Arrows on the optical transforms indicate lamellar repeat frequencies (dark, styrene; light, isoprene).

Figure 19 shows a region with the lamellae arranged in concentric rings. Notice that the lamellae perpendicular to the cutting direction have smaller spacings than those parallel to the cutting direction, in agreement with the results of Odell et al.[15]

Figure 20 shows an underfocus series of the *unstained* ISI copolymer. As predicted, the phase contrast is nearly absent in the zero-defocus image and increases with increasing defocus to give a simple lamellar image at 40-μm underfocus. The false half-fringes predicted in Figure 11 to occur at $\Delta Z = -10$ μm are indeed present in Figure 20. Because -10 μm is the optimum defocus for the third order, this reflection shows up in the optical transform as indicated by the outermost set of arrows. These half-fringes can also be seen in the microdensitometer tracing of the unstained micrographs (see Figure 21). Both the densitometer traces and the images show a significant amount of "noise". This noise arises from statistical density fluctuations in the polymer that are modulated by the pupil function. This dark and light speckle is present in defocus images of all amorphous materials and not only in polymers. The size of the speckle is determined by the

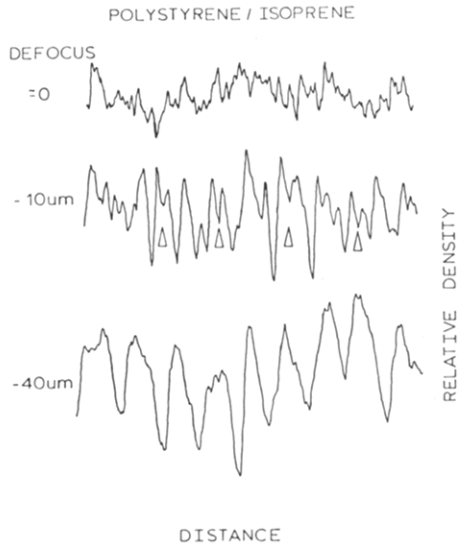

Figure 21. Microdensitometer scans of the images in Figure 20 (scans are not in vertical registry). Arrows point out weak half-spacings.

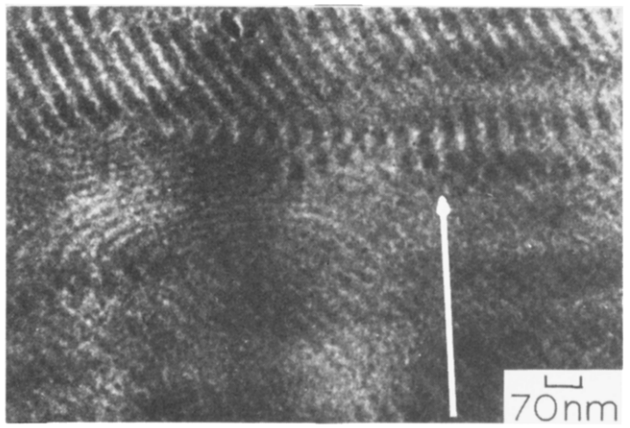

Figure 22. Defocus image of ISI lamellar copolymer. Arrow indicates microtoming direction.

range of spacings transferred by the pupil function; thus they increase in size with increasing defocus.

The variation in spacing of the lamellae with angle to the microtome knife is found in unstained sections as well (see Figure 22).

That the contrast seen in these defocus images is primarily phase contrast can be demonstrated by a series of micrographs taken at corresponding amounts of overfocus and underfocus (see Figure 23). The calculations above showed that there should be nearly exact reversal in the domain contrast on changing from overfocus to underfocus. Scattering contrast, however, is independent of defocus so that if significant scattering contrast is present, the domain structure will be visible in the zero-defocus image and the underfocus image should have enhanced contrast (scattering + phase) while the overfocus image should have decreased contrast (scattering − phase). Figure 23 shows that there is essentially no contrast at zero defocus and nearly exact inversion of contrast at large overfocus and underdefocus, confirming the absence of scattering contrast.

In a recent study of styrene–butadiene diblock copolymers containing a spherical polybutadiene phase, Berney et al. found the average sphere radius determined from EM of OsO_4-stained microtomed sections to be approximately 23% smaller than the value determined by small-angle neutron scattering.[23] The present method of imaging unstained, microtomed sections could perhaps

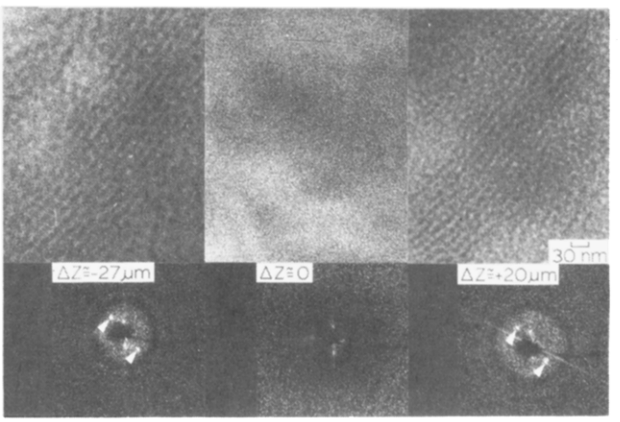

Figure 23. Through-focus series of ISI lamellar copolymer. Arrows on the optical transforms indicate lamellar repeat frequency.

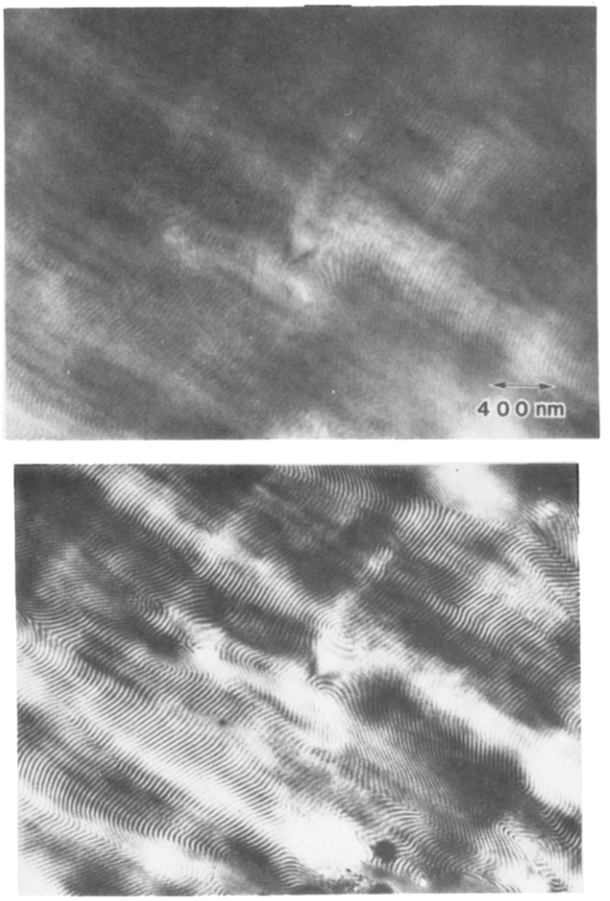

Figure 24. Defocus *unstained* (top) and infocus osmium tetraoxide *stained* (bottom) images of the same areas of ISI lamellar copolymer.

confirm the effect of OsO_4 staining on phase dimensions by direct EM examination. Because of the variability of domain dimensions (due primarily to microtome effects—see later discussion), the phase contrast (unstained) and scattering contrast (stained) images of the *same area* were compared by the following experiment: first a defocus image was taken with low electron dose, approximately 0.01 C/cm^2. The sample was taken out of the microscope and exposed to osmium tetraoxide vapor, and the same area reimaged at zero defocus. Figure 24 shows that both of these images exhibit the same features. (There is a slight increase in magnification with underfocusing of 0.06%/μm underfocus over the range 0 to −40 μm used in these experiments.) The lack of any appre-

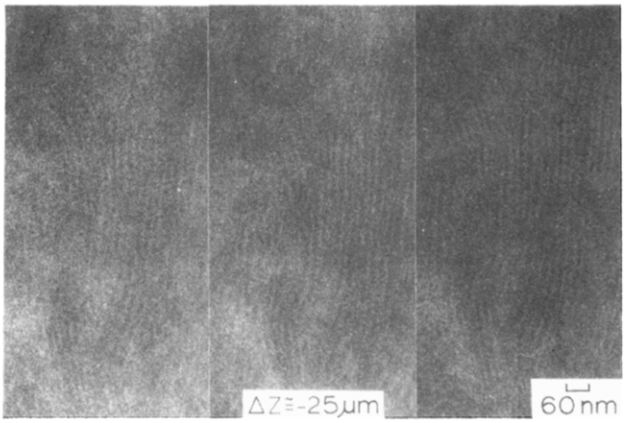

Figure 25. Successive defocus images of ISI lamellar copolymer as a function of electron dose: ~0.01 C/cm^2 (left); ~0.02 C/cm^2 (center); >1 C/cm^2 (right).

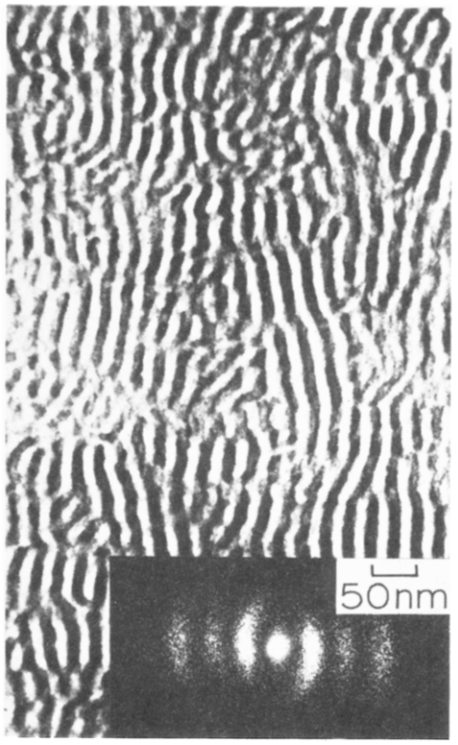

Figure 26. Osmium tetraoxide stained image of SBS lamellar copolymer.

ciable change in the domain structure from the staining process may be due to the prior cross-linking of the sample from the 0.01 C/cm^2 electron exposure and/or the difference between isoprene and butadiene as well as the different type of rubber domain (lamellar vs. spherical). Further careful work to sort out staining effects is certainly warranted.

Radiation Damage. The electron doses required to obtain a defocus series at a direct magnification of 20 000–33 000 are much higher than those generally recommended for polymer imaging. Although styrene, butadiene, and isoprene radiation damage primarily by cross-linking, even small relative chemical or density changes could result in significant differences in the mean inner potential difference between the phases from that in the undamaged copolymer. To monitor changes that might occur with increasing dose, a series of defocus micrographs (at the same defocus) of the ISI lamellar copolymer were taken at doses of ~0.01 C/cm^2 (see Figure 25, left), ~0.02 C/cm^2 (Figure 25, center), and very high dose, greater than 1 C/cm^2 (Figure 25, right). Only a minimal increase in the contrast level from the low dose to the high dose images is apparent, indicating that the mean inner potential difference between the two phases increases only slightly with dose.

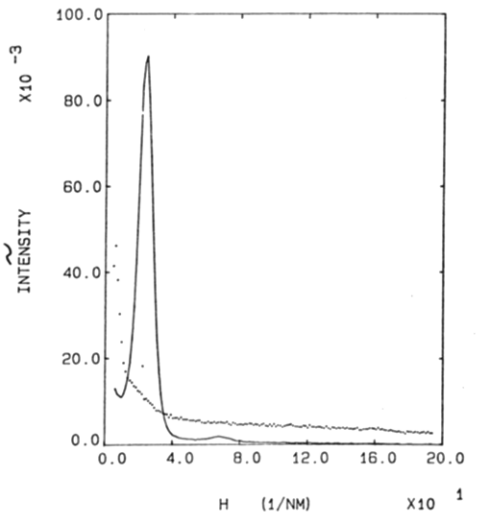

Figure 27. Smeared intensity vs. h. SAXS data from SBS lamellar copolymer taken with the beam parallel (solid line) and perpendicular (dotted line) to the film surface.

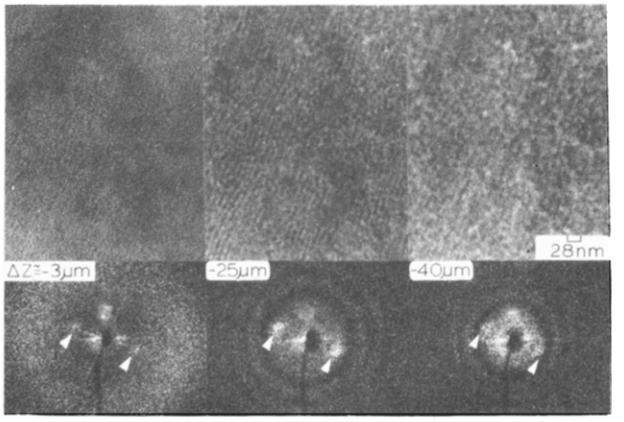

Figure 28. Defocus series of SBS lamellar copolymer at small defocus (left), nearly optimum defocus (center), and greater than optimum defocus (right). Arrows indicate lamellar repeat frequency position on the optical transforms.

SBS Lamellar Copolymer. Figure 26 is a BF micrograph of the osmium tetraoxide stained SBS triblock copolymer sectioned perpendicular to the film plane. Because this was a melt-pressed film, the lamellae are of short lateral extent and lie preferentially in the plane of the film. The SAXS patterns in Figure 27 taken with the X-ray beam parallel and perpendicular to the film surface confirm these results. The perpendicular pattern shows no scattering maxima, while the parallel pattern exhibits a very strong first-order peak at 28 nm and a much weaker third-order peak.

The phase contrast images of the SBS copolymer are similar to those for the ISI copolymer. Figure 28 is a defocus series of a region containing the smallest set of spacings found in this polymer, 14 nm, to emphasize the use of optimum defocus. The optimum defocus for a 14-nm-long period is reached at 22-μm underfocus. The contrast increases with defocus until optimum defocus and then decreases as the resolution becomes poorer than the long period (see Figure 28, right).

SIS Cylindrical Copolymer. As demonstrated by the SAXS pattern in Figure 14, the SIS cylindrical polymer was highly oriented in shear so that the direction of the

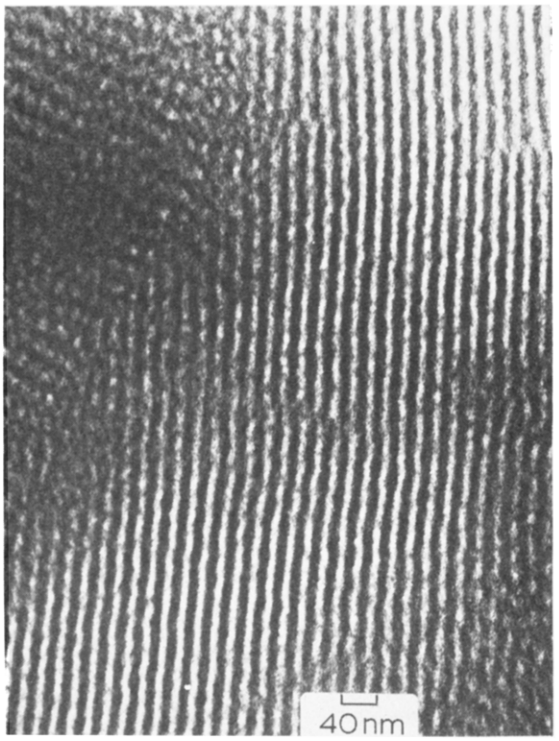

Figure 29. Longitudinal view of styrene cylinders (light) in an osmium tetraoxide stained isoprene matrix (dark).

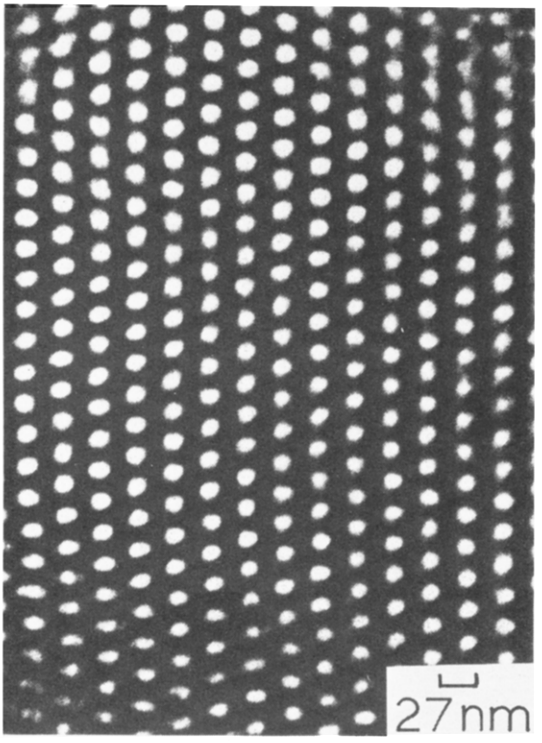

Figure 30. Transverse view of styrene cylinders (light) in an osmium tetraoxide stained isoprene matrix (dark).

cylinder axis was well defined. Therefore, the polymer could be microtomed in two directions to obtain transverse and longitudinal projections of the hexagonally packed cylinders. The images of the two projections of an osmium tetraoxide stained sample are shown in Figures 29 and 30. The d spacings of the hexagonal projection as measured by the optical diffraction were 23.5, 18.3, and 18.5 nm. The d spacing of the longitudinal projection was 18.5 nm. Again significant deformation is present in this copolymer, with the smaller d spacings being in the microtoming direction. Somewhat less variation was noted in the cylinder spacings than in the lamellar spacings, which is reasonable since the matrix is rubbery in the cylindrical copolymer.

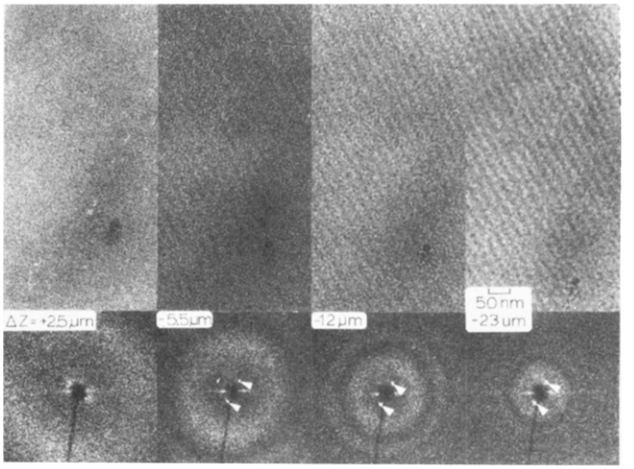

Figure 31. Defocus series of the longitudinal view of styrene cylinders (dark) in an *unstained* isoprene matrix (light). Arrows indicate cylinder repeat frequency.

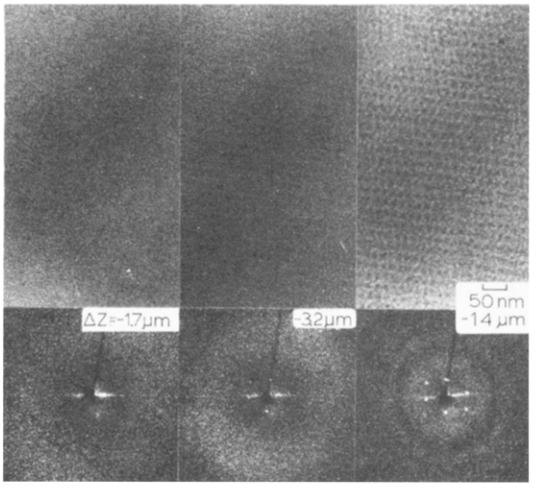

Figure 32. Defocus series of the transverse view of styrene cylinders (dark) in an *unstained* isoprene matrix (light).

The unstained longitudinal and transverse defocus series along with their optical transforms are shown in Figures 31 and 32, respectively. The d spacing for the longitudinal projection is 24.6 nm as measured from the optical transforms. The contrast is shown to increase with increasing defocus as predicted in Figure 17. The increase is size of the background dark–light speckle (from the statistical density fluctuation) with increased defocus is also quite apparent in Figure 31.

The transverse sections show a similar trend with defocus although the contrast is very low, probably due to tilt of the cylinders from the vertical direction of a few degrees. The optical transforms clearly show a significantly deformed hexagonal pattern with spacings of 21.3, 16.9, and 14.7 nm. All three of the spacings are smaller than those found by SAXS, indicating considerable compression in the plane of the film.

SI Star Copolymer. The osmium tetraoxide stained image for the 12-arm star in Figure 33 shows a large variation in phase size from 10 to 200 nm in diameter. Interestingly, the dispersed phase is isoprene, which is the core of the star and comprises 73 vol % of the material. The morphology of a series of star copolymers is currently being investigated and will be presented in a future paper.[21] The interest here is only the unstained phase contrast

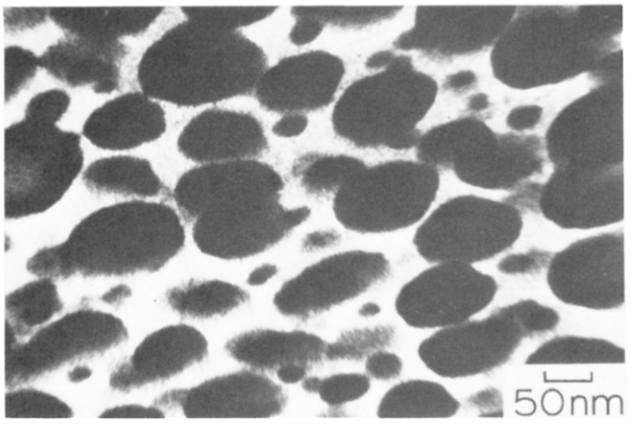

Figure 33. Osmium tetraoxide stained images of SI star copolymer. Dark regions are isoprene and the light matrix is styrene.

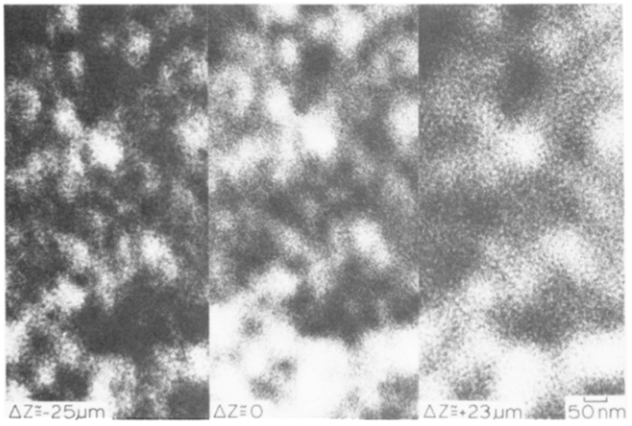

Figure 34. Through-focus series of thick film of *unstained* SI star copolymer exhibiting scattering contrast as well as phase contrast. Light regions are isoprene and the dark matrix is styrene.

imaging of the morphology. The unstained through-focus series is shown in Figure 34. Because the domains are much larger than those discussed above, simple projections can be obtained in thick sections so that the zero-focus image now exhibits discernible scattering contrast between the less dense isoprene domains (light) and the more dense styrene matrix (dark). In the presence of scattering contrast, Figure 34 shows that underfocus enhances the scattering contrast. Overfocus, however, produces phase contrast of the opposite sign working against the scattering contrast, thus decreasing the total contrast.

Conclusions

The technique of phase contrast imaging has been shown to be sensitive enough to small differences in composition to image *unstained* styrene–butadiene and styrene–isoprene block copolymers having lamellar, cylindrical, and spherical domains. Several features of the phase contrast images were predicted by model image calculations and confirmed experimentally:

(1) The center-to-center domain spacing (or long period) measured by phase contrast is independent of defocus and identical with that measured in stained images after correcting for a small increase in magnification for large underfocuses.

(2) The amount of contrast obtained depends on the mean inner potential between the phases but is also a strong function of defocus.

(3) The apparent domain profile observed by phase contrast imaging is mainly a function of defocus, interface width, and coherence of the electron beam. Caution should be used in interpreting images from periodic objects with phase structures other than 50/50 volume fractions: the phase size *will* be a function of defocus at large defocus!

(4) Determination of interface width and profile by phase contrast imaging is unlikely unless the inner potential difference is larger than that provided by most block copolymers. Polymer systems with such large inner potential differences would most probably exhibit sufficient scattering contrast for imaging without staining. This arises from the similarity in the effect of interface widths to other smoothing effects such as beam coherence, multiple scattering, and poor resolution at large defocuses where contrast is sufficient for imaging.

(5) At zero defocus, phase contrast is negligible and any residual scattering contrast can be observed. Where scattering contrast was present, the total contrast was shown to be increased by underfocusing and decreased by overfocusing.

An attempt was made to compare phase dimensions determined by microscopy before and after OsO_4 staining and EM results with results from SAXS. No appreciable change in phase dimensions with OsO_4 staining occurred for an ISI lamellar system. However, the deformation that occurred in microtoming was found to be substantial in all samples. Deformation was greatest for the sample with the polystyrene matrix, intermediate for the lamellar morphologies, and least for the sample with the isoprene matrix. This deformation precludes accurate comparison of the images with SAXS although the long periods found by SAXS did fall in the range of spacings found in the images.

The ability of phase contrast to image polymer phases of such similar composition and density without resorting to chemical modification of one or both phases has far-reaching applications in the growing field of phase-separated copolymer and blend morphology. One such application, the imaging of copolymers in which neither phase is readily stainable such as the styrene–hydrogenated rubber copolymers will be presented in a future paper.[22]

Acknowledgment. Financial support was from the NSF through Grant DMR-80-12724 (Polymers Program). The use of the facilities of the Materials Research Laboratory at the University of Massachusetts is also gratefully acknowledged.

Registry No. Styrene/isoprene copolymer, 25038-32-8; styrene/butadiene copolymer, 9003-55-8.

References and Notes

(1) J. Petermann and H. Gleiter, *J. Polym. Sci., Polym. Phys. Ed.*, **13**, 1939–1944 (1975).
(2) K. J. Hanszen, *Adv. Opt. Electron Microsc.*, **4**, 1–84 (1971).
(3) H. P. Erickson, *Adv. Opt. Electron Microsc.*, **5**, 163–199 (1973).
(4) D. L. Misell, "Image Analysis, Enhancement, and Interpretation"; North-Holland Publishing Co., Amsterdam, 1978.
(5) D. L. Misell, *Prin. Tech. Electron Microsc.*, **8**, 181–245 (1978).
(6) J. M. Cowley, "Diffraction Physics", North-Holland Publishing Co., New York, 1975.
(7) G. L. Christner and E. L. Thomas, *J. Appl. Phys.*, **48**, 4063–4067 (1977).
(8) E. J. Roche and E. L. Thomas, *Polymer*, **22**, 333–341 (1981).
(9) H. Kawai, T. Hashimoto, K. Miyoshi, H. Uno, and M. Fujimura, *J. Macromol. Sci., Phys.*, **B17**, 427–472 (1980).
(10) G. Hadziioannou and A. Skoulios, *Macromolecules*, **15**, 258–262 (1982).
(11) G. Hadziioannou and A. Skoulios, *Macromolecules*, **15**, 271–273 (1982).
(12) G. Hadziioannou and A. Skoulios, *Macromolecules*, **15**, 267–271 (1982).
(13) G. Hadziioannou, A. Mathis, and A. Skoulios, *Colloid Polym. Sci.*, **257**, 136–139 (1979).
(14) L. Bi and L. J. Fetters, *Macromolecules*, **9**, 732–742 (1976).
(15) J. A. Odell, J. Dlugosz, and A. Keller, *J. Polym. Sci., Polym. Phys. Ed.*, **14**, 861–867 (1976).

(16) N. G. Wrigley, *J. Ultrastruct. Res.*, **24**, 454–464 (1968).
(17) J. W. Cahn and J. E. Hilliard, *J. Chem. Phys.*, **28**, 258–267 (1958).
(18) E. Helfand and Y. Tagami, *J. Chem. Phys.*, **56**, 3592–3601 (1972).
(19) J. Petermann, private communication.
(20) D. L. Misell and I. D. J. Burdett, *J. Microsc. (Oxford)*, **109**, 171–182 (1977).
(21) D. L. Handlin, D. J. Kinning, D. B. Alward, L. J. Fetters, and E. L. Thomas, manuscript in preparation.
(22) D. L. Handlin and E. L. Thomas, submitted to *J. Mater. Sci.*
(23) C. V. Berney, R. E. Cohen, and F. S. Bates, *Polymer*, **23**, 1222 (1982).
(24) The use of the word "phase" in this paper will take three different meanings, depending on the context: (1) the phase of a wave of electrons; (2) phase contrast in the electron microscope; and (3) domains in polymers representing separate thermodynamic phases of material. Therefore, in order not to confuse the reader, effort has been made throughout the paper to provide a clear context.

Spectroscopic Study of Polystyrene and Poly(vinyl methyl ether) Blends

F. J. Lu, E. Benedetti, and S. L. Hsu*

Department of Polymer Science and Engineering, University of Massachusetts, Amherst, Massachusetts 01003. *Received November 3, 1982*

ABSTRACT: Various incompatible or compatible polystyrene and poly(vinyl methyl ether) blends have been prepared by varying composition, solvent, and thermal history. Fourier transform infrared spectroscopic analysis of these samples has revealed definite spectral features sensitive to compatibility. The vibrations most sensitive to change in molecular environment are the CH out-of-plane vibration in PS and the $COCH_3$ vibrations of PVME.

Introduction

Recently, there has been a large number of theoretical and practical studies attempting to better understand the phase separation behavior of polymer blends and the associated properties.[1] In our laboratory we have used primarily vibrational spectroscopy to characterize microstructures of polymer blends and their changes when samples are deformed macroscopically. These experiments, in conjunction with other physical measurements, are useful in the development of phenomenological models for deformation describing more fully the structure–property relationships of polymer blends. We have given particular attention to polystyrene (PS)/poly(vinyl methyl ether) (PVME) blends. The unusual compatibility behavior of this binary mixture is particularly interesting. A number of workers have shown that solvent, molecular weight, composition, and temperature can all affect the compatibility of these two polymers.[2-9]

Of all the possible binary mixtures, few are compatible. In these systems, favorable intermolecular interaction is a necessary requirement. However, in most cases the molecular origin of the driving force for compatibility is generally not clearly understood. Therefore, the search and characterization of molecular parameters lowering the total free energy represent important areas of study. Vibrational spectroscopy is an attractive technique for such studies. When properly assigned, the position, intensity, and shape of vibrational bands are useful in clarifying conformational and environmental changes of polymers at the molecular level. Because intrachain energy is so much higher than interchain nonbonded interactions, spectroscopic features of a single molecule as a result of molecular interaction are generally quite small. Strong interactions such as intermolecular hydrogen bonding are well documented in the literature. In most polymer blends, however, small differences in the vibrational spectra are difficult to observe directly and can only be shown in the difference spectra. The advent of Fourier transform infrared spectroscopy has made analysis of chemical mixtures by computer-calculated difference spectra quite convenient and accurate. As a result, several studies have shown specific spectroscopic features sensitive to changes in compatibility can be observed and have been used to interpret conformation or environment of polymers when blended.[10-17]

We have prepared compatible or incompatible PS/PVME films of various compositions from various solvents. In addition, phase-separated binary mixtures can be prepared at temperatures above the lower critical solution temperature (LCST). We have obtained infrared data from all these samples and have identified spectroscopic features characteristic of localized structure and environment of individual components in compatible or incompatible binary mixtures. Our results are reported here.

Experimental Section

Atactic PS and PVME used in this study were obtained from commercial sources. PS of weight-average molecular weight, M_w, 233 000 with polydispersity equal to 1.06 was obtained from Pressure Chemical Co. Other narrow molecular weight distribution atactic polystyrenes of M_w = 175 000, 50 000, and 37 000 were obtained from Polysciences. PVME was also obtained from Polysciences. Its molecular weights (M_w = 99 000, M_n = 46 000) were determined by GPC in our laboratory. In this case, polystyrene was used as standard. We found PVME as purchased contained a strong band at 1735 cm^{-1}. This vibration has been assigned to the C=O group stretching vibration of butethal, which can be removed by vacuum desiccation. Solvents of spectral grade were obtained commercially and used without further purification.

Thin films of the PS/PVME binary mixtures (15, 50, 64, and 84% weight fraction of PS) were prepared from solutions (approximately 3–5% by weight) by casting onto potassium bromide (KBr) windows. Compatible films were obtained from toluene solutions. Incompatible ones were cast from chloroform or trichloroethylene. The solvents were completely removed by drying in vacuum ovens at 70 °C for at least 72 h. It has been suggested that morphology of the samples may be affected by differences in concentration, extreme thinness of film prepared, and solvent evaporation rate.[5] Furthermore, band shape and relative intensities can depend on index of refraction due to dispersion effects.[13] We tried to remedy these experimental errors by preparing films under identical conditions. Thermally induced phase-separated samples were prepared by keeping the thin film on KBr in the oven at appropriate temperatures.

Infrared spectra were obtained with a Nicolet 7199 Fourier transform infrared instrument. Three hundred scans of 2-cm^{-1} resolution were signal averaged and stored on a magnetic disk

0024-9297/83/2216-1525$01.50/0